Investigating unconventional superconductivity in the 2D Hubbard-Kanamori model using Functional Renomarlization Group (FRG)

210003218

February-May 2025

Contents

1 Abstract

2 Introduction

3 Theoretical Background

3.1 Unconventional superconductivity

For many years after the discovery of superconductivity in 1911 [1] physicists were convinced that BCS-Eliashberg-electron-phonon theory [2] provided a complete explanation of the pairing mechanism in all superconducting materials. However, in 1986, the discovery of the first heavy-fermion superconductor [3] resulted in the emergence of a whole new class of materials: Unconventional Superconductors. These are condensates of cooper pairs formed by a **different** pairing mechanism than the electron-phonon coupling predicted by BCS theory [4].

Most generally, the Hamiltonian for a superconducting state can be described as follows:

$$\hat{H} = \hat{H}^0 + \hat{H}^{cp} \tag{1}$$

where $\hat{H}^{cp}$ describes the pairing interation that leads to the formation of a Cooper pair and is given by:

$$\hat{H}^{cp} = \sum_{k,k'} \Gamma(k,k') c_{k,\uparrow}^\dagger c_{k',\downarrow}^\dagger c_{k',\uparrow} c_{-k,\downarrow} \tag{2}$$

For many unconventional superconductors, the form of the effective pairing interaction $\Gamma(k,k')$ has remained as an unanswered question for decades.

3.1.1 Spin-fluctuation mediated superconductivity

One emerging theory for some unconventional superconductors such Iron-based or heavy-fermion compounds is that underlying pairing mechanism is driven by spin fluctuations [5]. This section discusses how to model spin-fluctuation mediated superconductivity for the fluctuation-exchange approximation(FLEX) [6].

In such cases, the effective pairing interaction $\Gamma(k, k')$ is given by [1]:

$$\Gamma(k, k') = \frac{3}{2}U^2\chi^S(k - k') - \frac{1}{2}U^2\chi^C(k - k') + U \tag{3}$$

This equation is taken from Ref. [7]. Here, U is the on-site Coulomb repulsion and χ^S, χ^C are the interacting spin-susceptibilities in the Charge (C) and Spin(S) channel respectively. Their form is given below.

$$\chi^S(q) = \frac{\chi^0(q)}{1 - U\chi^0(q)} \tag{4}$$

$$\chi^C(q) = \frac{\chi^0(q)}{1 + U\chi^0(q)} \tag{5}$$

These interacting spin susceptibilities are expressed in terms of the non-interacting dynamic spin susceptibility (χ^0_{ps}) which is stated below without formal proof [5].

$$\chi^0_{ps}(q, i\omega) = -\sum_k \int_0^\beta d\tau G^0_{ps}(k + q\tau)G^0_{sp}(k, -\tau)e^{i\omega\tau} \tag{6}$$

The calculations presented in this project are carried out in the spin-fluctuation framework. Whilst this theory has managed to succesfully capture key features in phase diagrams of unconvential superconductors, it also has its limitations. The most relevant example is that of the cuprate phase diagram. Spin-fluctuation theory is able to capture the superconducting dome and the correct order parameter [8,9] but fails to describe the characteristic pseudo-gap [10].

3.2 Hubbard-Kanamori Model

3.2.1 Tight Binding Models

The Tight Binding Model is a central element of condensed matter physics (7). In this model, electrons are bound in orbitals (called sites) around the lattice ions. Due to the overlap between the quantum mechanical wavefunctions that describe these sites, electrons are allowed to 'hop' to neighbouring sites. The probability that this hopping process will occur is given by a tunnelling amplitude, which can be calculated using a hopping integral.

This work is carried out in the tight-binding model framework, where the magnitude of the tunnelling amplitudes are at first treated as free parameters. Here, we build from a simple

---

[1]Note that this form of pairing interaction assumes that the ratio between the fluctuation frequence w_f and the Fermi energy is small.

2D nearest-neighbour hoppping Hubbard model (Section. 3.2.2) and investigate the effect of introducing and varying the strength of the next-nearest neighbour hopping amplitude (See Fig. 1). We extend these models further by considering the two-orbital per site case.

$$\hat{H}_{TB}(\underline{R}) = \sum_{ij\sigma} t_{ij}(\hat{c}_{i\sigma}^\dagger \hat{c}_{j\sigma} + h.c) \tag{7}$$
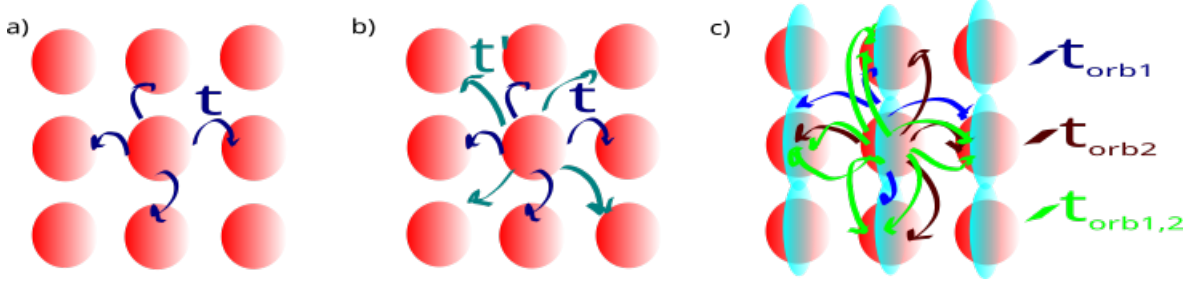
Figure 1: **Two-Dimensional Tight-Binding Models:** Three pannels showing the tight binding models for the 1NN, 1NNN and 1NN2 models discussed in Section 5.1, 5.2 and 5.3 respectively. Fig a) shows the Nearest-neighbour hopping case, where t depicts the hopping amplitude between the neighbouring sites. Fig b) shows the inclusion of the next-nearest neighbour hopping-magnitude given by t'. Fig c) Shows the extension to the two-orbital case, depicting same orbital (t_{orb1}, t_{orb2}) and different orbital ($t_{orb1,2}$) nearest-neighbour hopping. Note that this is just a pictorial representation of the orbitals, and that it does not correspond to a particular choice of orbitals or their real space projection.

3.2.2 Hubbard Model

The tight binding model as defined above fails to account for any interactions between neighbouring electrons. This motivates the extension of this model to the Hubbard model (8), which includes the (onsite) Coulomb repulsion between electrons. Despite its simple form, this model can describe very rich physical phenomena. In particular, it becomes very interesting to study when U and t are of comparable order, since it highlights the competing phenomena that takes place in correlated systems. The 2D Hubbard model remains unsolved to date, but is able to predict all sorts of correlated phases: it describes metals, insulators, superconductors and other exotic phases [11–14]. This model has been widely studied since it resembles the structure of the cuprate high-temperature superconductors [15].

$$\hat{H} = \sum_{ij\sigma} -t_{ij}(\hat{c}_{i\sigma}^\dagger \hat{c}_{j\sigma} + h.c) + U \sum_i \hat{n}_{i\uparrow} \hat{n}_{i\downarrow} \tag{8}$$

3.2.3 Hubbard-Kanamori Model

In the case of materials with a multi-band and/or multi-orbital nature, the Hubbard model is not sufficient to capture all of the physical phenomena. This motivates the extension of the Hubbard Model to the Hubbard-Kanamori model [16] by including a Hund's coupling term.

$$H_{int} = U \sum_{is} n_{i,s\uparrow} n_{i,s\downarrow} + \frac{V}{2} \sum_{i,s,t\neq s} n_{is} n_{it} - \frac{J}{2} \sum_{i,s,t\neq s} \vec{S}_{is} \cdot \vec{S}_{it} + \frac{J'}{2} \sum_{i,s,t\neq s} \sum_\sigma c_{is\sigma}^\dagger c_{is\bar\sigma}^\dagger c_{it\bar\sigma} c_{it\sigma} \tag{9}$$

Here, U and V represent the electronic interactions in the same and different orbitals respectively. For generality, the intraorbital exchange J and the 'pair hopping' term J' following from Hund's rule coupling have been separated. Note that this Hamiltonian is relevant for the later section of this project, where the model is extended to a two-orbital, two-dimensional Hubbard Model.

3.3 Theoretical Background in FRG

Solving the Hubbard-Kanamori Hamiltonian is rather challenging, which is why we resort to numerical techniques such as FRG to do so. FRG falls into the category of many other weak-coupling techniques (such as Mean field-theory [17], pertubation theory [18], Density Functional theory [19] or Random Phase approximation [20]). In these theories, interactions between electrons are considered to be weak. This allows one to effectively model the electrons in the system as free particles and treat their interactions as a pertubation. In the non-interacting limit, the method is therefore exact. Beyond this limit, it is controlled by the ratio between the interaction strength and the bandwidth of the system.

In this section the theoretical framework in which FRG calculations are performed is outlined. The central element of FRG is a flow equation that describes the evolution of the effective action of the system with respect to a scalar/flow parameter Lambda Λ *(See section 3.3.1)*. The flow equation can be solved exactly for a limited number of systems, so for most scenarios an approximation has to be made in order to reach a solution in a reasonable computational

time. More details of how this approximation is performed and the limitations it presents can be found in Section 3.3.2. For the systems explored in this project only two-particle interactions are considered and any higher order terms are neglected. This allows for the effective action of the system to be separated into three terms, which correspond to three physical channels: Superconductivity, Spin-Density and Charge-Density Waves. The calculation is then performed to determine the "winning channel" which will correspond to the respective physical phase that the model exhibits. This rather "hand-wavy" overview of FRG is represented in a flowchart in Fig.2. For a more rigorous explanation the reader is referred to the sections below.
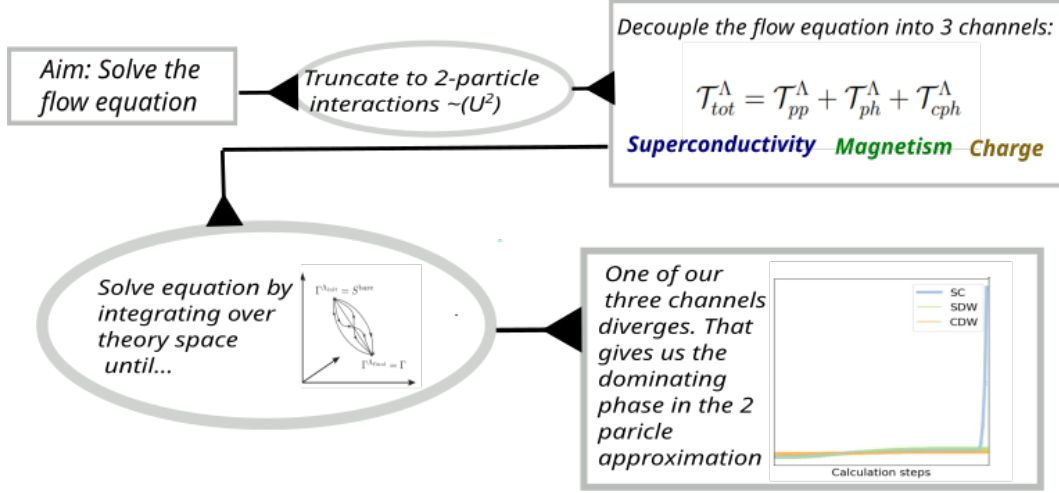

Figure 2: **FRG Flowchart:** Schematic diagram outlining the TU^{2}FRG calculation steps. Starting from the flow equation and applying the truncation scheme in order to decouple the action into three "physical" terms. The flow equation can then be solved by calculating each channel separatedly and taking the dominating phase to be the channel that diverges.

3.3.1 Flow equation

In this section the derivation of the flow equation is outlined. For such, it is assumed that the reader has grasped a strong understanding in Quantum Field theory and many-body physics. If interested in the finer details of the derivation, the reader is refferred to [21].

The central elements of statitiscal physics are the partition function, the canonical potential and its Legendre transformations. These are such powerful physical quantities that one can derive all physical observables from them. For quantum many-body problems, one works instead with partition functional, defined as follows in Eq.10:

$$\mathcal{Z}[\bar{\eta}, \eta] = \int \mathcal{D}\bar{\psi}\mathcal{D}\psi e^{\mathcal{S}[\bar{\psi}, \psi]} e^{(\bar{\eta}, \psi) + (\eta, \bar{\psi})} \tag{10}$$

In the case of fermionic systems, the action in the exponent of Eq.10 takes the form shown below.

$$\mathcal{S}[\psi, \bar{\psi}] = -(\bar{\psi}, G_0^{-1}\psi) + V[\psi, \bar{\psi}] \tag{11}$$

Here, $V[\psi, \bar{\psi}]$ is an arbitrary many-body interaction and G_0 represents the propagator of the non-interacting system. This equation contains the shorthand notation (...), which represents the sum $\sum_x \bar{\psi}(x)(G_0^{-1}\psi)(x), (G_0^{-1}\psi)(x) = \sum_{x'} G_0^{-1}(x, x')\psi(x')$. In this sum, the Grassman field index x represents all the quantum numbers of the single-particle basis and imaginary time.

Note that in the limiting case where $V = 0$, the path integral in Eq.10 is exactly solveable. However, once electronic correlations are included, the picture becomes more complicated. The main idea behind FRG is to introduce a cut-off in the non interacting Green's function ($G_0 \rightarrow G_0^\lambda = f(\lambda)G_0$). This cutoff is then interpolated between the solveable intital state and the full path integral solution by susbsequently including electronic interactions. For a spin-independant system this would transform the bare propagator as shown in Equations (12) and (13).

$$G_0(k_0, \mathbf{k}) \rightarrow G_0^\lambda(k_0, \mathbf{k}) \tag{12}$$

$$\frac{1}{ik_0 - \xi_{\mathbf{k}}} \rightarrow \frac{\theta^{\mathbf{k}}}{ik_0 - \xi_{\mathbf{k}}} \tag{13}$$

where $\theta^\lambda(\mathbf{k})$ is defined, for example, as follows:

$$\theta^\lambda(\mathbf{k}) = \Theta(|\xi_{\mathbf{k}}| - \lambda) \tag{14}$$

With this cutoff scheme, the calculation then excludes points close to the Fermi Surface as shown in Figure (FIGURE).
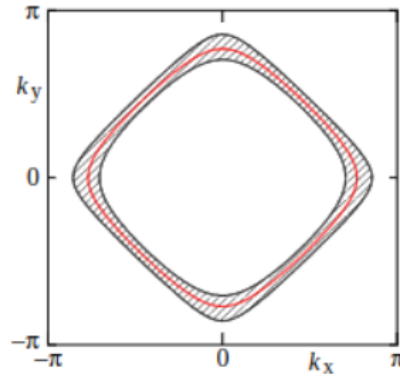
Figure 3: **Cut-off scheme example:** Momentum space region(shaded in grey) around the Fermi-surface(red) that is excluded by a momentum cut-off for a 2D square lattice with a lattice constant of 1Å. Taken from [21]

.

In the following steps the derivation will proceed in the framework of the so-called "effective action" ($\mathcal{T}[\psi, \bar{\psi}]$). This is the Legendre transformation of the Greens function functional ($\mathcal{G}[\eta, \bar{\eta}]$),

defined below in Equations (15, 16) and (17) respectively. *(For convinience and for reasons that are beyond the scope of this project it is more convinient to work with the effective action than it is to do so with the partition functional.)* [2]

$$\mathcal{G}[\eta, \bar{\eta}] = -ln(\mathcal{Z}[\eta, \bar{\eta}]) \tag{15}$$

$$\mathcal{G}[\eta, \bar{\eta}] = -ln \int \mathcal{D}\psi \mathcal{D}\bar{\psi} e^{-\mathcal{S}[\psi, \bar{\psi}]} e^{(\bar{\eta}, \psi) + (\bar{\psi}, \eta)} \tag{16}$$

$$\mathcal{T}[\psi, \bar{\psi}] = (\bar{\eta}, \psi) + (\bar{\psi}, \eta) + \mathcal{G}[\eta, \bar{\eta}] \tag{17}$$

The next step is to introduce a scalar flow parameter λ into the generating functionals defined above. This is done in the same manner as is outlined in the example shown in Equations (12, 13). But more generally, has to be performed such that the generators recover their orginal structure at $\lambda = 0$. After a series of algebraic manipulations, which are ommitted here but can be found in [21], one arrives at the exact functional flow equation for the effective action:

$$\frac{d}{d\Lambda} \mathcal{T}^{\Lambda}[\psi, \bar{\psi}] = (\bar{\psi}, \dot{Q}_0^{\Lambda} \psi) - \frac{1}{2} \text{tr}\big(\dot{Q}_0^{\Lambda}(\mathbf{\Gamma}^{(2)\Lambda}[\psi, \bar{\psi}])^{-1}\big). \tag{18}$$

Where $\Gamma^{(2)\lambda}[\psi, \bar{\psi}]$ and $\underline{Q}_0^{\Lambda}$ are given by equations (19) and (20) respectively.

$$\Gamma^{(2)\lambda}[\psi, \bar{\psi}] = \begin{bmatrix} \bar{\delta}\delta\Gamma[\psi, \bar{\psi}](x', x) & \bar{\delta}\bar{\delta}\Gamma[\psi, \bar{\psi}](x', x) \\ \delta\delta\Gamma[\psi, \bar{\psi}](x', x) & \delta\bar{\delta}\Gamma[\psi, \bar{\psi}](x', x) \end{bmatrix} \tag{19}$$

$$\underline{Q}_0^{\Lambda} = \begin{bmatrix} Q_0^{\Lambda} & 0 \\ 0 & -Q_0^{\Lambda t} \end{bmatrix} = diag(Q_0^{\Lambda}, -Q_0^{\Lambda t}), \tag{20}$$

This equation, as mentioned previously, is the central element of FRG and the sections below outline how to solve it.

3.3.2   Truncation scheme (TU^{2}FRG)

The flow equation derived above can be solved for a limited amount of systems. However, in most cases, the memory demand for the FRG calculations is high. In order to tackle this issue, the truncated unity approximation (TU^{2}FRG) was introduced in 2020 [22]. The main idea behind this scheme is to find a new basis that, with a controlled loss of accuracy, can represent all of the required elements in a compressed way. It can be shown [23], that such a basis can be constructed and is well defined in the case where the calculation is constrained to terms U^2 *(two-particle interactions)*. Partitions of unity [3] are then introduced into a specific part of the flow equation. This reduces an otherwise computationally expensive nested integral to a matrix product. Details of how this truncation is incorporated are ommitted but the reader is referred to Appendix. (REFERENCE appendix).

---

[2]If interested in why see REFERENCE

[3]A detailed explanation of what these are can be found in [23]

Whilst the truncated scheme presents advantages in computational efficiency, particularly for models with broken translational symmetry, it also has its limitations. TU²FRG relies on short-range interactions, thus struggling to capture strongly correlated phases. This is particularly relevant for the study of the 2D Hubbard model. TU²FRG will not be able to capture the characteristic Mott insulating phase of the Cuprate phase diagrams [24], which limits how well the results presented in this project can be directly compared with existing literature. More importantly, the truncation scheme has a direct consquence on the accuracy of the predicted phase transition temperature (T_c), it is able to correctly capture the trends in T_c but the values predicted are much higher than what is sensible to expect in real materials. Nevertheless, TU²FRG manages to successfully capture the competition between Magnetic and Superconducting instabilities, which is one of the main focus of the results presented here.

3.3.3 Decoupling of flow equation

After constraining ourselves to the case of two-particle interactions in the framework of translationally invariant systems, one can decouple the evolution of the two-particle coupling as a function of the flow parameter λ into three channels:

$$V(k1, k2, k3) = V^{(0)}_{k_1,k_2,k_3} - \phi^P_{k_1+k_2, \frac{k_1-k_2}{2}, \frac{k_4-k_3}{2}} + \phi^C_{k_1-k_3, \frac{k_1+k_3}{2}, \frac{k_2+k_4}{2}} + \phi^D_{k_3-k_2, \frac{k_1+k_4}{2}, \frac{k_2+k_3}{2}} \tag{21}$$

Here, the three channels correspond to a particle-particle, crossed particle-hole and (three) direct particle-hole terms given explicitly below in terms of the respective effective actions. They represent all possible ways in which the two particle interactions can occur in the correlated system. The particle-particle (P), cross-particle-hole (C) and direct-particle-hole (D) channels correspond to the Superconducting, Charge and Magnetic phases respectively.

$$\dot{\phi}^P_{k_1+k_2, \frac{k_1-k_2}{2}, \frac{k_4-k_3}{2}} = -\mathcal{T}_{pp}(k1, k2, k3) \tag{22}$$

$$\dot{\phi}^C_{k_1-k_3, \frac{k_1+k_3}{2}, \frac{k_2+k_4}{2}} = -\mathcal{T}_{cr-ph}(k1, k2, k3) \tag{23}$$

$$\dot{\phi}^D_{k_3-k_2, \frac{k_1+k_4}{2}, \frac{k_2+k_3}{2}} = -\mathcal{T}_{d-ph}(k1, k2, k3) \tag{24}$$

This effectively allows one to treat the effective action as a separable object:

$$\mathcal{T}[\psi, \bar{\psi}] = \mathcal{T}_{pp}[\psi, \bar{\psi}] + \mathcal{T}_{ph}[\psi, \bar{\psi}] + \mathcal{T}_{cph}[\psi, \bar{\psi}] \tag{25}$$

3.3.4 Instability calculation

The procedure from the decoupled effective action and flow equation is outlined here. For more details the reader is refferred to [25]. A FRG calculation will return the self-energy and two-particle vertex [4]. These quantities are not directly experimentally accessible, so a series of post

---

[4] An exact definition of these can be found in [21], but is omitted here.

processing steps have to be carried out. The first step is to find out which of the three channels diverge. This gives the diverging susceptibility. Mean-Field analysis is then carried out at the critical scale in order to obtain the ordering symmetry and a linearised gap equation. The later allows one to calculate the Superconducting gap and order parameter.

4   Computational Methods

This section outlines how the concepts presented above link together and are implemented for the purpose of this project. The general aim is to solve the 2D Hubbard-(Kanamori) model. This is achieved computationally, using the divERGe package (See section 4.2) which implements the TU^{2}FRG formalism discussed in the section above. All of the calculations are carried out under the assumption that the superconductivity is spin-fluctuation mediated. This section outlines the methods followed to calculate the required Tight-Binding Models for each of the systems, the utilisation of Diverge to solve them and some of the utilised post-processing techniques.

4.1   Tight-Binding Models

This project discusses three models: the 1NN, 1NNN and 1NN2 model (*See Fig.1*). For the first two, the hopping parameters in the tight-binding model are treated as free parameters. For the later, the hopping parameters are determined using the method described below.

Constrained to the case of a single layer, the 1NN model is extended to a multi-orbital system by including two-orbitals per site and investigating the effect of the interorbital hopping. To allow for comparison with existing literature [26], a $d_{x^2-y^2}$ and $d_{3z^2-r^2}$ orbital are included. Their respective hopping parameters are determined using the table of interatomic matrix elements calculated by J.C. Slater and G.F. Koster [27]. In this calculation, the values of the σ, π, δ bond strength are approximated to $\approx 1, 0.5, 0.05eV$ respectively in order to capture their relative values [28–30]. A table summarising estimated parameters for the models discussed in Section 5.3 is shown below.

Model	$t^{[1,0,0]}_{3z^2-r^2}$	$t^{[0,1,0]}_{3z^2-r^2}$	$t_{x^2-y^2}$	$t^{[1,0,0]}_{x^2-y^2-3z^2-r^2}$	$t^{[0,1,0]}_{x^2-y^2-3z^2-r^2}$
	-0.781	-0.719	-0.375	-0.402	-0.310
1NN2MN	on	on	on	off	off
1NN2MY	on	on	on	on	on

Table 1: **Nearest neighbour hopping parameters for 2D two-orbital Hubbard models.** First row shows the calculated hopping parameters. Other rows show which hopping parameters were included in each of the two models.

4.2   divERGe

divERGe is an open-source, high-performance, C/C++/Python library that includes a truncated unity FRG (TU^{2}FRG) computational backend [31]. Under the approximations outlined in Section3.3.2, the flow equations are integrated fromhigh scales($\lambda = \inf$) to low scales ($\lambda = 0$)

by numerically going from λ to $\lambda + d\lambda$. This integration is repeated until a phase transition (divergence of one of the calculated channels) occurs or a minimal λ is reached. In the later case, the system is assumed to be in a Fermi-Liquid state. All calculations have been carried out in the HPC cluster at the university of St Andrews.

4.3 Convergence of Calculation

In the truncated-unity approximation there are several convergence tests that one needs to carry out in order to verify that the calculations are accurate. These include the form factor convergence and the number of k points.

4.3.1 Form factor convergence

The set of orthogonal basis functions (f_m) used to describe the Truncated space*(See section 3.3.2)* in momentum representation is called the **form factors**. In the case of the square lattice, these take the form of delta functions in real space. The form factors are arranged as circles with increasing radii around the origin. This effectively leads to a "bond-like" representation where the form-factor number essentially determines how many of the neighbouring bonds are accounted for in a calculation for each point. This is depicted in Fig. . For mathematical rigour on the definition of the form factor, the reader is referred to [23].

The divERGe package allows the user to modify the number of form-factor shells accordingly. It boils down to a trade between computational accuracy and expensiveness. For the results in this project, the form factor value was set at 4Å^5. The convergence of the calculations was tested accordingly for a range of points in the phase diagram (an example is shown in Fig.4). Moreover, this is in agreement with values used in previous literature [23].
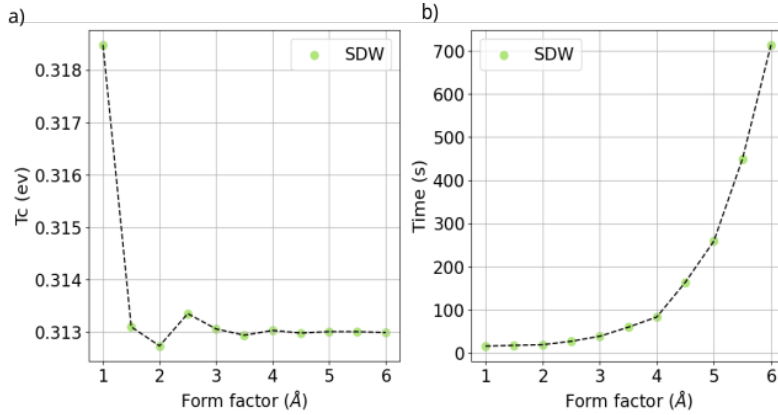

Figure 4: **Convergence testing:** Fig a) Transition temperature as a function of form factor for the 1NN model, U = 5.00, $\mu = 0.20$eV. Fig b) Time taken for calculation as a function of form factor.

---

[5]This is equivalent to a number of form factor shells of 4 since the lattice spacing of the models here is set to 1Å.

4.3.2 Number of k points convergence

When integrating the flow equation, there are two parameters that can be further tuned to ensure convergence. Those are n_k and n_{k_f} and loosely speaking specify the number of k points used to carry out the nested integrations. In particular, n_k refers to the number of k points used for the general momentum integral, and n_{k_f} for the additional sum around each k-point. The calculations performed here were carried out with an integration grid of 20x5 (n_k x n_{k_f}) points. The choice of parameters ensured that the calculations had converged appropriatedly and resulted in a computational time of $\approx 180s$ per point.

4.4 Calculation of Susceptibilities

4.4.1 Nesting vectors

4.4.2 Superconducting order parameters

5 Results and discussion

5.1 1NN Model

We define the 1NN model as the 2D Hubbard model with a single orbital per site, allowing hopping between nearest-neighbour sites *(a diagramatic representation can be found in Fig.1.a)*. As outlined in Section 3.2.2, solving this model near half-filling becomes a hard endeavour. This section explores the solution to the 1NN Model Hamiltonian using two-particle-interaction-truncated FRG. Here, a phase diagram in terms of the on-site Coulumb repulsion U and chemical potential μ is presented and discussed in detail. The calculations were carried out using a 20x5 n_kxn_{kf} grid and a form factor of 4Å, with a nearest-neighbour hopping parameter of 1eV. The choice of convergence parameters was determined by the methods discussed in Section 4.3. Results are presented for Coulumb repulsion values ranging from 1-20 eV and chemical potential values spanning the entire energetic bandwith of the model (from -4eV to 4eV). Whilst there exists previous work on the 2D Hubbard Model using FRG [32–34] most of it focuses on specific areas of the phase diagram. Thus, very limited investigation has been carried out on the effect of varying the on-site Coulumb repulsion. Therefore, the work presented here covers a much wider range of parameters than what has previously been explored.

There are several caveats to the results presented here. In real materials, the chemical potential is an easily tuneable parameter due to its strong connection to the electronic doping of the system. In turn, controlling the magnitude of the Coulumb repulsion between electrons is by no means straightforward. Moreover, some of the interesting features discussed in this report lie outside of the physical regime. (ie- in our FRG calculation a weak-coupling limit was assumed and therefore any Coulumb repulsion values above the magnitude of the bandwidth of the material (8eV) can be considered to be unphysical in this limit.) Therefore, the analysis performed in this project does not neccesarily provide a route to enhance the superconductivity in the materials that resemble the models investigated. Instead, the main aim is to understand how varying certain parameters *(U, μ, t')* affects the correlated phases observed in the model. It is also important to note, as discussed in Section 3.3.2, that any analysis on the transition temperature

of the superconducting regions must be treated qualitatively and that this work does not claim to have found Superconducting regions with transition temperatures of the order of thousands of Kelvin.

The complete phase diagram for the values discussed above is shown in Fig.5. As is expected for both the Hubbard model and the Cuprates [35–37], a strong competition between Magnetism and Superconductivity (SC) is observed. This results in the emergence of a magnetic dome, sandwiched between two narrower d-wave superconducting regions. This magnetic dome is **Anti-Ferromagentically** (AFM) ordered and its width increases as the magnitude of the Coulumb repulsion is increased. A greater Coulumb repulsion thus favours the magnetic instability as the "winner" of this competition for a larger range of doping values. Since both the AFM and d-wave SC are driven by repulsive scattering between $(\pi,0)$ and $(0,\pi)$ vectors, their competition is at its largest closest to the Van-Hove singularity, where both grow and reinforce the other [38,39]. Moreover, narrow magnetic stripes appear for even integer chemical potential values. For large values of U *(those that exceed the material's bandwidth)* there are patches of a charge density wave instability sorrounding the superconducting regions.

The findings presented here are consistent with other studies of the two-dimensional Hubbard model. Dynamical Mean Field Theory(DMFT) has previously captured the coexistance of the AFM and SC order parameter within the same solution for a range of doping*(μ in the findings here)* at weak-coupling. A smooth transition between these two phases has also been observed [40]. However, the FRG 2D 1NN Hubbard model fails to capture Mott insulating phases or the formation of the pseudo-gap [41, 42], both of which are characteristic to the Cuprate phase diagram.

5.1.1 Superconductivity in the 1NN Model

Recent findings have claimed that the 2D Hubbard model does not have a superconducting ground state [43]. Whilst the model in Ref. [43] is the same as the 1NN model explored in this section, their analysis is conducted in a slightly different framework than the one used in this project: using DMRG [44] at moderate-strong coupling and for values of U between 6-8eV*(which they claim to be the regime relevant to the cuprates)*. The lack of superconductivity in their findings is attributed to a lack of competition between the magnetic and superconducting phases. Here, in the weak-coupling framework both a competition between magnetism and superconductivity and a stabilised superconducting region is found. The superconducting order parameter for this stable region is plotted on top of the Fermi-Surface for the first BZ (Fig.6a). The order parameter shows antisymmetry with respect to a 90 degree rotation and therefore one concludes that the superconducting region is d-wave symmetric. This is in agreement with what is expected from the Cuprate superconductors [45].

After plotting the the critical temperature (Tc) as a function of chemical potential (μ) for a constant Coulumb repulsion(U), one observes that the superconducting critical temperature is maximised closest to the magnetic instability (Fig.6b). This is in agreement with the idea that competition between instabilities enhace the phase transition temperature [46, 47]. Moreover, the magnitude of the Coulumb repulsion and Tc are positively correlated, as is to be expected from the assumed of the pairing mechanism*(See Eq.3)*. It is important to note that limiting the
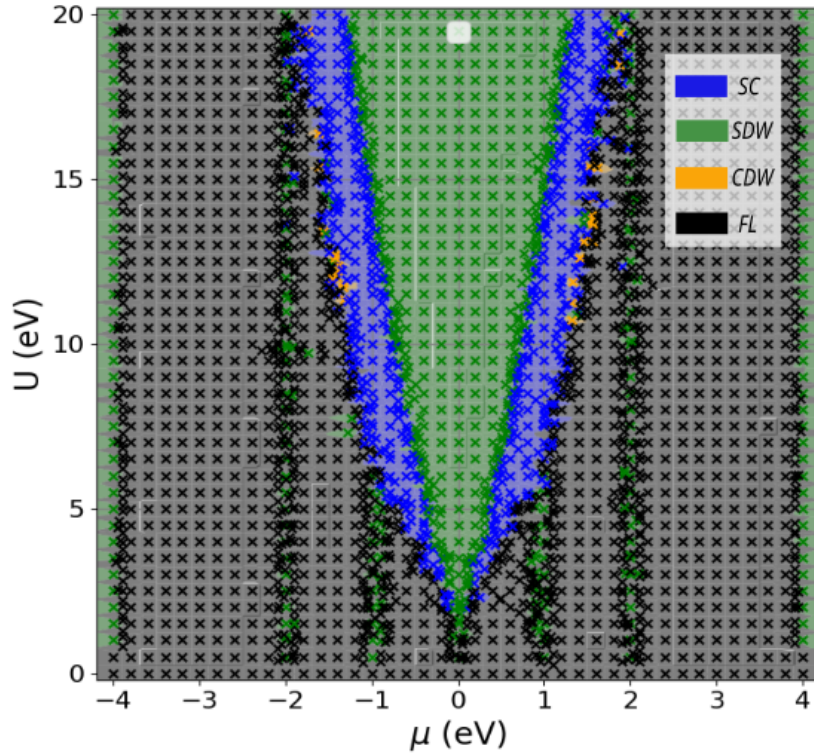
Figure 5: **Phase diagram for the 1NN model**: (t =1eV, nkxnkf = 20x5, ff = 4Å) as a function of On-site Coulumb Repulsion U and chemical potential μ. Figure shows the four phases observed in the 1NN model: SC (Superconductivity), SDW (Spin-Density Wave), CDW(Charge Density Wave) and FL (Fermu-Liquid). Calculated points in the phase diagram are showed by the 'x' markers and a lighter-couloured background is used to depict interpolated regions between these points.

interactions accounted for in the FRG calculation to two-particle interactions acts as a bottle-neck for the accuracy of the Tc values calculated. Nevertheless, the trends in Tc remain trustworthy.
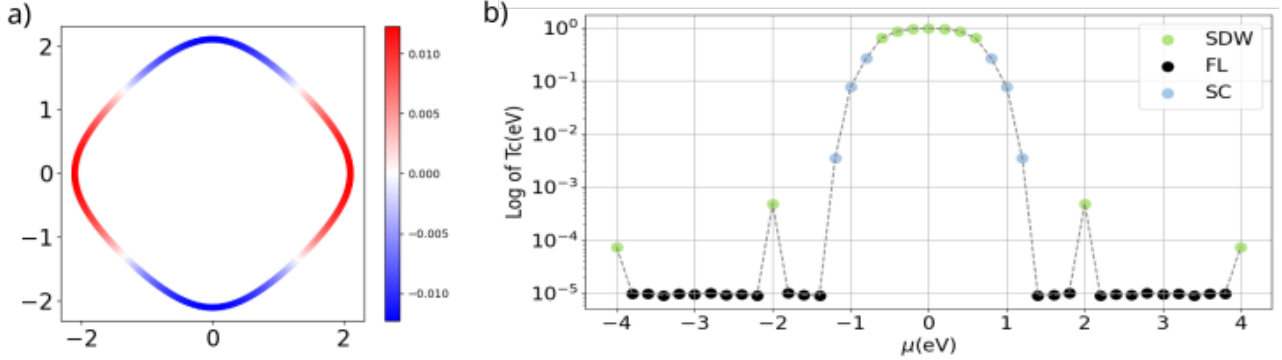

Figure 6: **Superconductivity in the 1NN model**: Fig a) Superconducting order parameter projected on Fermi Surface at $\mu = 1.00$ eV, for U =10.00eV. The order parameter is antisymmetric about a 90 degree rotation and hence it exhibits d-wave symmetry. Fig b) Transition temperature (Tc) plotted on a logarithmic scale as a function of chemical potential (μ) for U =10.00eV. Tc is enhanced closest to the magnetic instability. Although both plots are shown only specific for certain values of U and μ, the results they display hold for the enterity of the superconducting region of the phase diagram in Fig.5.

5.1.2 Magnetic stripes in the 1NN Model

Another distinctive feature of the Cuprates *(as well as other unconventional superconductors* [48]*)* is the emergence of "stripes". These are patterns of alternating charge-density and spin density waves [49,50]. In the 1NN model discussed here, such stripes are not observed. Nevertheless, one finds magnetic regions of interest outside of the main Anti-Ferromagnetic dome. The 1NN phase diagram in Fig.5 shows what will from now on be reffered to as a "magnetic stripe" occuring at even integer values of chemical potential(μ). These "magnetic stripes" are thin magnetic regions that occur in parallel domains and for very specific values of chemical potential. Most of them are Ferromagnetically ordered and evolve to some commensurate nesting vector as the Coulumb repulsion is increased. However, the physics becomes more interesting for a chemical potential of $\mu = 1.00eV$. In the Cuprates, $\frac{1}{8}$th is reffered to as the magical doping [51]. The doping value recieves its name from the emergence of stripe ordering and supresion of superconductivity. Here, the magical doping corresponds to a chemical potential of $\pm 1.00eV$($\frac{1}{8}$th of the bandwidth). One observes that for low Coulomb repulsion values there is a Ferromagenctically ordered SDW. This SDW is then supressed by a Superconducting Phase and is later recovered at around $\approx U = 15.00eV$. This second SDW state is now Antiferromagnetically ordered. The T_c increases along the stripe(Fig.7). Whilst not quite the conventional stripe behaviour observed in the Cuprates, it is safe to conclude that there is still something "magical" about a $\frac{1}{8}$th filling fraction in the 1NN model presented here. It is important to note that before carrying out this analysis the possibility of the stripes being a result of a computational artefact was ruled out. This was done by increasing the n_kxn_{k_f}-resolution for a single point in the stripe and verifying that the

15

result of the calculation does not change. The appearance of these stripes as true results of the calculations is further confirmed in Section 5.2.2.
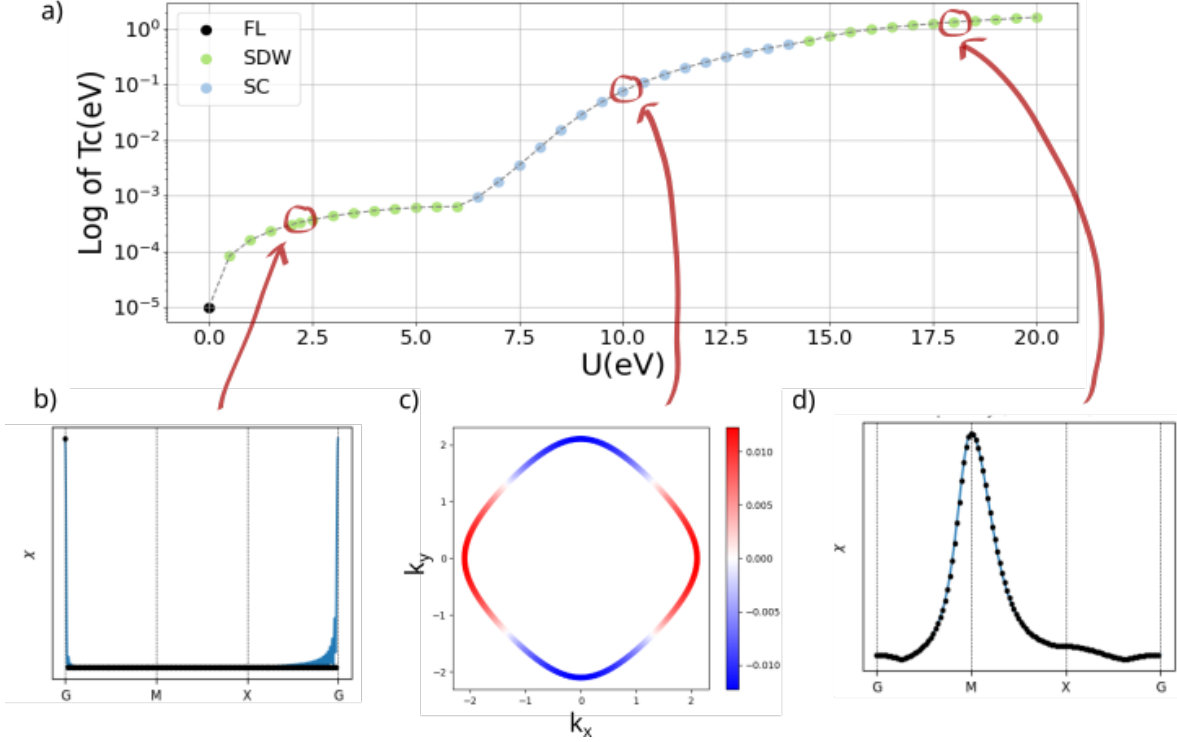

Figure 7: **Magntic stripe in the 1NN model for doping at $\frac{1}{8}$ of the bandwith**: Fig a) Transition temperature plotted in a Logarithmic scale as a function of Coulumb repulsion (U) along the Magnetic stripe at μ =1eV. Fig b) Magnetic susceptibility along high symmetry path for U =2.00 eV. Fig c) Plot of the Superconducting order parameter projected on top of the Fermi-surface of the 1NN model for U = 10.00eV and μ =1.00eV. Fig d) Magnetic susceptibility along high symmetry path for U= 18.00eV. Plots showing the susceptibility as a function of $\underline{q}$ for both magnetic regions. The Ferromagnetic SDW is supressed by a superconducting phase at U≈ 6.00eV. At larger values of U, the SDW phase is recovered but with an Anti-Ferromagnetic ordering instead.

5.2 Effect of next-nearest neighbour hopping (1NNN model)

The 1NNN model is defined as the extension of the 1NN model described above, with the inclusion of the next-nearest neighbour hopping amplitude as a free parameter. This section discusses three additional phase diagrams for the two-dimensional Hubbard model with a respective next-nearest neighbour hopping amplitude of 0.25, 0.50 and 0.75 eV(Fig.8). The nearest neighbour hopping amplitude is maintained at 1eV for all models. Moreover, the chemical potential of the models is set accordingly to ensure a constant number of electrons at half-filling so that the models are comparable.

As the next-nearest neighbour hopping is increased the position of the Van-Hove singularity

16

is lowered in energy. Increasing t' also changes the Fermi-surface and therefore the nesting vectors of the models. As a result of both, when t' is increased, the magnetic-superconducting sandwich region is displaced towards the negative chemical potential regime. However, there are several features of the 1NN model that remain once t' is included. The superconducting regions remain (in the most-part) d-wave symmetric and one can still observe the emergence of magnetic stripes. Moreover, general trends in T_c are also observed: it is maximised closest to the magnetic instability and it increases as a function of U.

There have been several studies investigating the effect of t' in the 2D Hubbard model, both using FRG [52] and other alternative methods [53], with a particular focus on using the value t' as a route to enhance T_c. The results presented here are of a slightly different flavour, the aim is to compare the features of the 1NN and 1NNN phase diagrams.
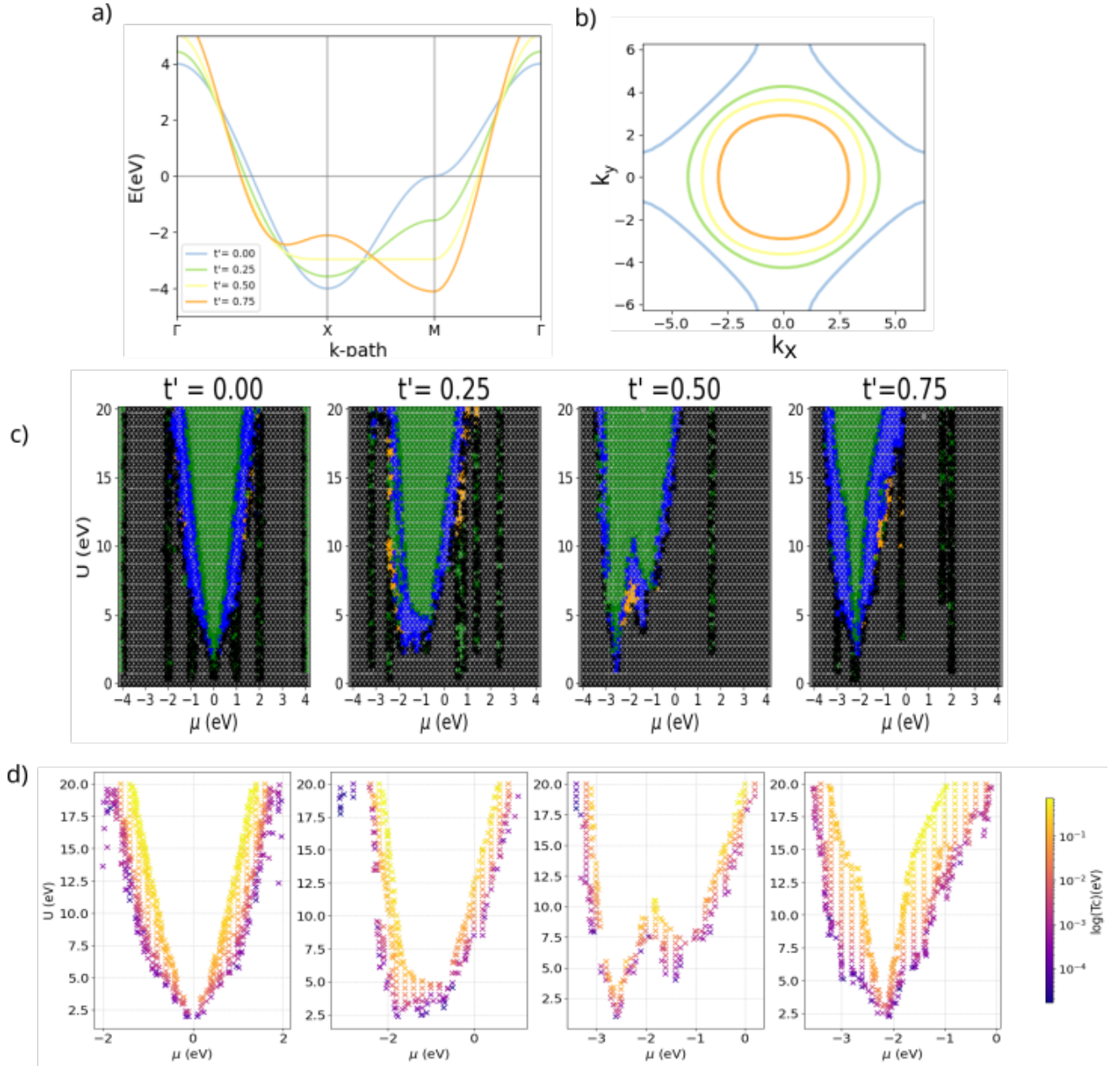
Figure 8: **1NNN model:** a) Single plot of the band structure along high-symmetry path for corresponding values of t'. b) Single plot of the Fermi surface for all values of t' considered. c) Phase diagram for the 1NNN model as a function of Coulumb repulsion U and chemical potential μ (t =1eV, nkxnkf = 20x5, ff = 4Å) for t'=0.00, 0.25, 0.50, 0.75 eV. d) Transition temperature for the superconducting region (plotted in a logarithmic scale).

5.2.1 Superconductivity in the 1NNN Model

Including a next-nearest neighbour hopping parameter in the 1NN model does not result in many changes of the superconductivity of the model. The order parameter is mostly d-wave symmetric and the T_c increases as a function of Coulumb repulsion. The proximity to a Magnetic instability enhances the superconducting transition temperature. Moreover, the same SC-SDW-SC sandwich is observed after breaking particle-hole symmetry. This supports the claim that SC is favoured in the vicinity of a SDW instability.

Whilst most key features remain the same, there are some important differences. In the case where $t' \neq 0$, CDW patches appear in the vicinity of SC regions. When $\frac{t'}{t} = 0.75$, and for all values of U between 8-11eV, the Superconducting order parameter changes. Along these horizontal cuts there is a SCI-SDW-SCII-CDW transition. The Superconducting order parameter is always d-wave symmetric in the SCI region and for most of the SCII region. It abruptly transitions to s-wave symmetric in the vicinity of the CDW region *(See Fig.9)*. This behaviour is also observed in the SC regions that neighbour CDW regions for the $t' = 0.25, 0.50eV$ models. In order to verify whether this corresponds to a physical phase transition, one should be able to experimentally observe a discontinuity as a consequence of an additional symmetry breaking when the order parameter changes from s- to d- wave symmetric.
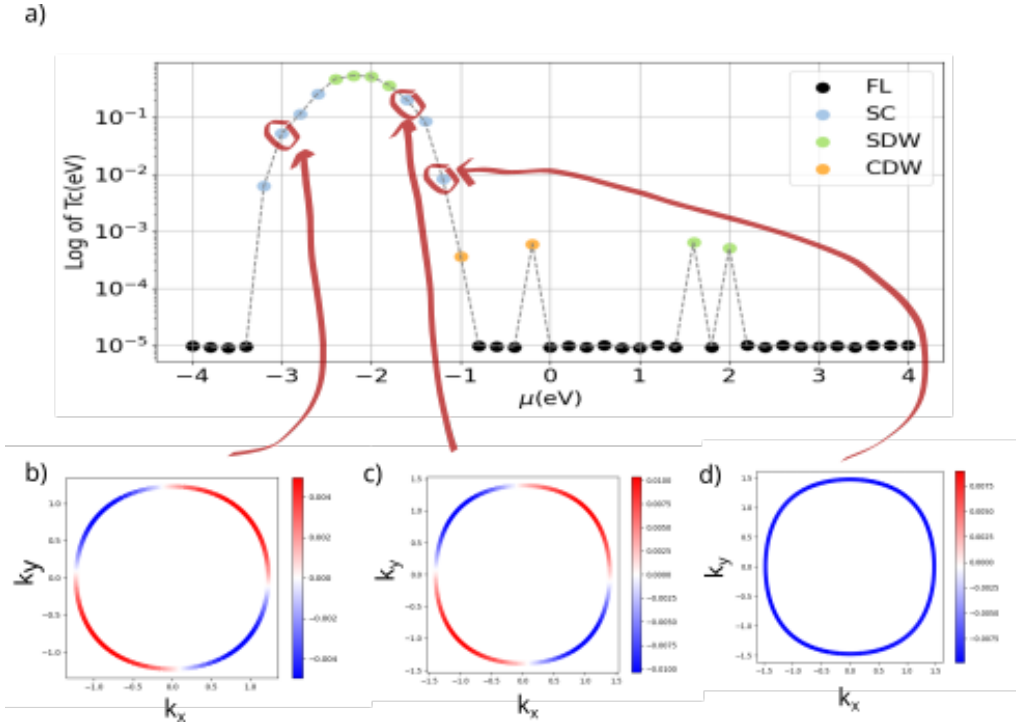

Figure 9: **Change in the superconducting order parameter in the t' =0.75eV 1NNN model**: Fig a) Critical temperature plotted in a Logarithmic scale as a function of chemical potential μ for U = 11.50eV. The lower panel shows the magnitude of the superconducting order parameter plotted on top of the fermi surface for U= 11.50eV and $\mu = $ -3.0eV, -1.6eV and -1.2eV. These are shown in Figs b) c) and d) respectively.

5.2.2 Magnetic stripes in the 1NNN model

The appearance of Magnetic stripes is another common denominator between the 1NN and 1NNN models, further reinforcing their physical origin. A survey of all stripes and their respective nesting vectors can be found in Table.2. The location of the stripes suggest that their emergence is a consequence of strong nesting at particular chemical potential values. The stripe at "magic doping" remains the only to have change ordering from FM to AFM as a consequence of the interplay with Superconductivity.

Whilst the transition from a Fermi-Liquid phase to any of a SC,SDW or CDW is quite abrupt, the critical temperature evolves more smoothly for those stripes which have a strong competition between SC and SDW/CDW instabilities *(See Fig.10)*. This is in agreement with that discussed in Section 5.1.2. When $\frac{t'}{t} = 0.50$, a magnetic double dome emerges, becoming more pronounced as the magnitude of the Coulomb repulsion increases *(See Fig.11)*. This is the pattern that one would have expected in the superconducting region(as is seen for the Cuprates [54]). However, this is the only model and phase for which this trend is observed.

t'(eV)	μ (eV)	Competing with other phase?	Nesting vector	Magnetic ordering
0.00	1.00	Yes (SC)	(0,0)-(π, π)	FM-AFM
0.00	2.00	No	(0,0)-(0, π)	FM-Commensurate
0.25	-3.20	No	(0,0)	FM
0.25	-2.40	No	(0,0)	FM
0.25	-2.00	No	(0,0)-(π, π)	FM - AFM
0.25	0.60	No	(0,0)	FM
0.25	1.40	Yes (CDW)	(0,0)	FM
0.25	2.40	No	(0,0)	FM
0.50	-2.60	No	(0,0)	FM
0.50	1.60	No	(0,0)	FM
0.75	-3.00	Yes(SC)	(0,0)	FM
0.75	-2.20	Yes(SC)	(0,0)-inc.	FM- Incommensurate
0.75	2.00	No	(0,0).	FM

Table 2: **Survey of stripes in the 1NNN model.** Table summarising the location and magnetic ordering of the Stripes in the 1NNN model .
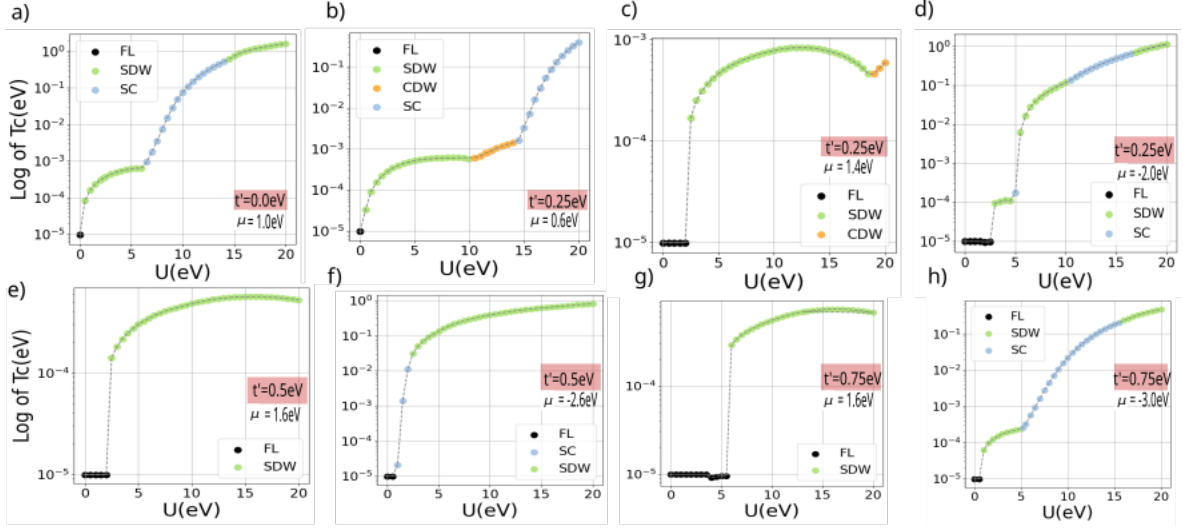
Figure 10: **Tc as a function of Coulomb repulsion for a selection of stripes in the 1NNN model**: Tc plotted in a logarithmic scale for stripes at: Fig a) t' = 0.00eV, μ=1.00eV, b) t' = 0.25eV, μ=0.60eV, c) t' = 0.25eV, μ=1.40eV, d) t' = 0.25eV, μ=-2.00eV, e) t' = 0.50eV, μ=1.60eV, f) t' = 0.50eV, μ=-2.60eV, g) t' = 0.75eV, μ=1.60eV, h) t' = 0.75eV, μ=-3.00eV
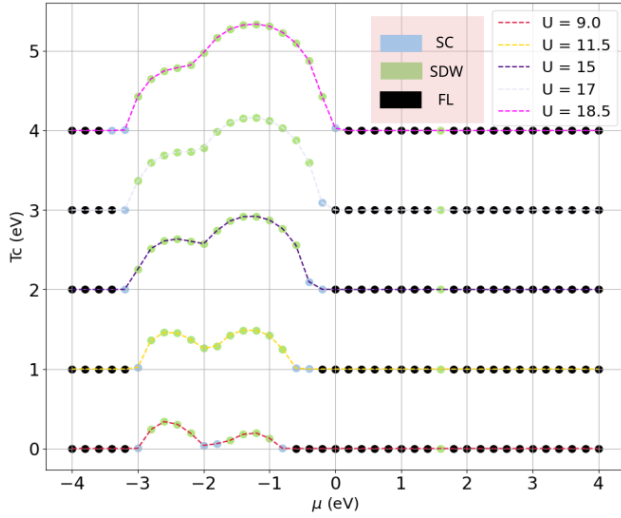

Figure 11: **Magnetic Dome in 1NNN, t'=0.50eV model**: Tc as a function of μ for different values of U (offsetted by 1eV). This figure shows how the height of the second magentic dome increases as a function of U whilst the height of the first remains constant. The turning point for the double dome pattern occurs at μ=-2.00eV

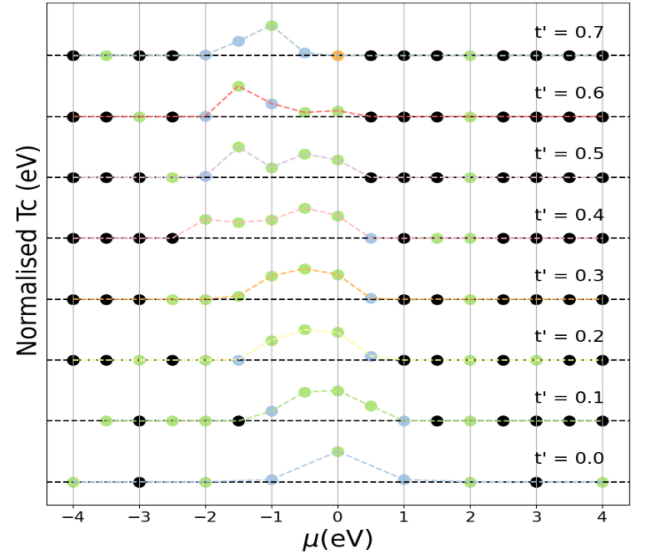Figure 12: **Continuous variation of t':** Normalised Tc plotted as a function of chemical potential μ for several values of t'. Tc is normalised separatedly with respect to the maxima of each plot in order to allow for the clear vizualisation of the trend.

5.3   Effect of bi-orbital system (1NN2 model)

6   Conclusion and Outlook

References

[1] H Kamerlingh Onnes. The superconductivity of mercury. *Comm. Phys. Lab. Univ. Leiden*, 122:124, 1911.

[2] J Robert Schrieffer. *Theory of superconductivity*. CRC press, 2018.

[3] J George Bednorz and K Alex Müller. Possible high t c superconductivity in the ba- la- cu- o system. *Zeitschrift für Physik B Condensed Matter*, 64(2):189–193, 1986.

[4] JE Hirsch, MB Maple, and F Marsiglio. Superconducting materials classes: Introduction and overview, 2015.

[5] Toru Moriya and Kazuo Ueda. Spin fluctuations and high temperature superconductivity. *Advances in Physics*, 49(5):555–606, 2000.

[6] Gökhan Esirgen and NE Bickers. Fluctuation-exchange theory for general lattice hamiltonians. *Physical Review B*, 55(4):2122, 1997.

[7] AB Migdal. Interaction between electrons and lattice vibrations in a normal metal. *Sov. Phys. JETP*, 7(6):996–1001, 1958.

[8] Toru Moriya. Developments of the theory of spin fluctuations and spin fluctuation-induced superconductivity. *Proceedings of the Japan Academy, Series B*, 82(1):1–16, 2006.

[9] Douglas J Scalapino. The case for dx2- y2 pairing in the cuprate superconductors. *Physics Reports*, 250(6):329–365, 1995.

[10] Tom Timusk and Bryan Statt. The pseudogap in high-temperature superconductors: an experimental survey. *Reports on Progress in Physics*, 62(1):61, 1999.

[11] Steven R White, Douglas J Scalapino, Robert L Sugar, EY Loh, James E Gubernatis, and Richard T Scalettar. Numerical study of the two-dimensional hubbard model. *Physical Review B*, 40(1):506, 1989.

[12] Jorge E Hirsch. Two-dimensional hubbard model: Numerical simulation study. *Physical Review B*, 31(7):4403, 1985.

[13] Philip W Anderson. "luttinger-liquid" behavior of the normal metallic state of the 2d hubbard model. *Physical review letters*, 64(15):1839, 1990.

[14] Kai Sun, Zhengcheng Gu, Hosho Katsura, and S Das Sarma. Nearly flatbands with nontrivial topology. *Physical review letters*, 106(23):236803, 2011.

[15] Elbio Dagotto. Correlated electrons in high-temperature superconductors. *Reviews of Modern Physics*, 66(3):763, 1994.

[16] Alexei Sherman. Hubbard-kanamori model: spectral functions, negative electron compressibility, and susceptibilities. *Physica Scripta*, 95(9):095804, 2020.

[17] Leo P Kadanoff. More is the same; phase transitions and mean field theories. *Journal of Statistical Physics*, 137:777–797, 2009.

[18] Naoto Nagaosa. *Quantum field theory in condensed matter physics.* Springer Science & Business Media, 2013.

[19] Walter Kohn and Lu Jeu Sham. Self-consistent equations including exchange and correlation effects. *Physical review*, 140(4A):A1133, 1965.

[20] David Bohm and David Pines. A collective description of electron interactions. i. magnetic interactions. *Physical Review*, 82(5):625, 1951.

[21] Walter Metzner, Manfred Salmhofer, Carsten Honerkamp, Volker Meden, and Kurt Schönhammer. Functional renormalization group approach to correlated fermion systems. *Reviews of Modern Physics*, 84(1):299–352, 2012.

[22] Christian J Eckhardt, Carsten Honerkamp, Karsten Held, and Anna Kauch. Truncated unity parquet solver. *Physical Review B*, 101(15):155104, 2020.

[23] Julian Lichtenstein. *Functional renormalization group studies on competing orders in the square lattice.* PhD thesis, Dissertation, RWTH Aachen University, 2018, 2018.

[24] Masatoshi Imada, Atsushi Fujimori, and Yoshinori Tokura. Metal-insulator transitions. *Reviews of modern physics*, 70(4):1039, 1998.

[25] Jonas Benedikt Profe. *Functional renormalization group developments for correlations in quantum materials.* PhD thesis, Dissertation, RWTH Aachen University, 2023, 2023.

[26] Hirofumi Sakakibara, Naoya Kitamine, Masayuki Ochi, and Kazuhiko Kuroki. Possible high t c superconductivity in la 3 ni 2 o 7 under high pressure through manifestation of a nearly half-filled bilayer hubbard model. *Physical Review Letters*, 132(10):106002, 2024.

[27] John C Slater and George F Koster. Simplified lcao method for the periodic potential problem. *Physical review*, 94(6):1498, 1954.

[28] Stephen J Blanksby and G Barney Ellison. Bond dissociation energies of organic molecules. *Accounts of chemical research*, 36(4):255–263, 2003.

[29] John E McGrady. Introduction and general survey of metal–metal bonds. *Molecular Metal-Metal Bonds: Compounds, Synthesis, Properties*, pages 1–22, 2015.

[30] Andreas Krapp, Matthias Lein, and Gernot Frenking. The strength of the σ-, π-and δ-bonds in re 2 cl 8 2-. *Theoretical Chemistry Accounts*, 120:313–320, 2008.

[31] Jonas Profe, Dante M Kennes, and Lennart Klebl. diverge implements various exact renormalization group examples. *SciPost Physics Codebases*, page 026, 2024.

[32] Jacob Beyer, Jonas B Profe, Lennart Klebl, Tilman Schwemmer, Dante M Kennes, Ronny Thomale, Carsten Honerkamp, and Stephan Rachel. Rashba spin-orbit coupling in the square-lattice hubbard model: A truncated-unity functional renormalization group study. *Physical Review B*, 107(12):125115, 2023.

[33] Cornelia Hille, Fabian B Kugler, Christian J Eckhardt, Yuan-Yao He, Anna Kauch, Carsten Honerkamp, Alessandro Toschi, and Sabine Andergassen. Quantitative functional renormalization group description of the two-dimensional hubbard model. *Physical Review Research*, 2(3):033372, 2020.

[34] Demetrio Vilardi, Pietro M Bonetti, and Walter Metzner. Dynamical functional renormalization group computation of order parameters and critical temperatures in the two-dimensional hubbard model. *Physical Review B*, 102(24):245128, 2020.

[35] Steven A Kivelson, Eduardo Fradkin, and Victor J Emery. Electronic liquid-crystal phases of a doped mott insulator. *Nature*, 393(6685):550–553, 1998.

[36] Eduardo Fradkin, Steven A Kivelson, and John M Tranquada. Colloquium: Theory of intertwined orders in high temperature superconductors. *Reviews of Modern Physics*, 87(2):457–482, 2015.

[37] Tuomas I Vanhala and Päivi Törmä. Dynamical mean-field theory study of stripe order and d-wave superconductivity in the two-dimensional hubbard model. *Physical Review B*, 97(7):075112, 2018.

[38] Nobuo Furukawa, TM Rice, and Manfred Salmhofer. Truncation of a two-dimensional fermi surface due to quasiparticle gap formation at the saddle points. *Physical review letters*, 81(15):3195, 1998.

[39] Carsten Honerkamp and Manfred Salmhofer. Temperature-flow renormalization group and the competition between superconductivity and ferromagnetism. *Physical Review B*, 64(18):184516, 2001.

[40] Massimo Capone and G Kotliar. Competition between d-wave superconductivity and antiferromagnetism in the two-dimensional hubbard model. *Physical Review B—Condensed Matter and Materials Physics*, 74(5):054513, 2006.

[41] AA Katanin, A Toschi, and K Held. Comparing pertinent effects of antiferromagnetic fluctuations in the two-and three-dimensional hubbard model. *Physical Review B—Condensed Matter and Materials Physics*, 80(7):075104, 2009.

[42] Junya Otsuki, Hartmut Hafermann, and Alexander I Lichtenstein. Superconductivity, antiferromagnetism, and phase separation in the two-dimensional hubbard model: A dual-fermion approach. *Physical Review B*, 90(23):235132, 2014.

[43] Mingpu Qin, Chia-Min Chung, Hao Shi, Ettore Vitali, Claudius Hubig, Ulrich Schollwöck, Steven R White, Shiwei Zhang, and (Simons Collaboration on the Many-Electron Problem).

Absence of superconductivity in the pure two-dimensional hubbard model. *Physical Review X*, 10(3):031016, 2020.

[44] Steven R White. Density matrix formulation for quantum renormalization groups. *Physical review letters*, 69(19):2863, 1992.

[45] CC Tsuei and JR Kirtley. Pairing symmetry in cuprate superconductors. *Reviews of Modern Physics*, 72(4):969, 2000.

[46] M Brian Maple. Interplay between superconductivity and magnetism. *Physica B: Condensed Matter*, 215(1):110–126, 1995.

[47] JP Sun, K Matsuura, GZ Ye, Y Mizukami, M Shimozawa, Kazuyuki Matsubayashi, M Yamashita, T Watashige, Shigeru Kasahara, Y Matsuda, et al. Dome-shaped magnetic order competing with high-temperature superconductivity at high pressures in fese. *Nature communications*, 7(1):12146, 2016.

[48] Barbara Goss Levi. Are stripes a universal feature of high-t c superconductors? *Physics Today*, 51(6):19–22, 1998.

[49] Oron Zachar, SA Kivelson, and VJ Emery. Landau theory of stripe phases in cuprates and nickelates. *Physical Review B*, 57(3):1422, 1998.

[50] Matthias Vojta. Lattice symmetry breaking in cuprate superconductors: stripes, nematics, and superconductivity. *Advances in Physics*, 58(6):699–820, 2009.

[51] Seiki Komiya, Han-Dong Chen, Shou-Cheng Zhang, and Yoichi Ando. Magic doping fractions for high-temperature superconductors. *Physical review letters*, 94(20):207004, 2005.

[52] Christoph Husemann and Walter Metzner. Incommensurate nematic fluctuations in the two-dimensional hubbard model. *Physical Review B—Condensed Matter and Materials Physics*, 86(8):085113, 2012.

[53] Rodrigo A Fontenele, Natanael C Costa, Thereza Paiva, and Raimundo R dos Santos. Effects of next-nearest neighbor hopping on the pairing and critical temperatures of the attractive hubbard model on a square lattice. *arXiv preprint arXiv:2503.06753*, 2025.

[54] Louis Taillefer. Scattering and pairing in cuprate superconductors. *Annu. Rev. Condens. Matter Phys.*, 1(1):51–70, 2010.